AAS 09-122

AUTONOMOUS OPTICAL LUNAR NAVIGATION

Brian Crouse,* Renato Zanetti,† Chris D'Souza‡ and Pol D. Spanos§

The performance of optical autonomous navigation is investigated for spacecraft in low lunar orbits and highly elliptical lunar orbits. Various options for employing the camera measurements are presented and compared. Strategies for improving navigation performance are developed and applied to the Orion vehicle lunar mission.

INTRODUCTION

Autonomous navigation in proximity to the Moon presents challenges not encountered in near-Earth navigation. The most obvious difference is the absence of GPS as a possible measurement. During the Apollo era, navigation relied on tracking and state updates from the ground. The Orion program, however, is required to navigate autonomously from the ground. Due to the absence of an atmosphere on the Moon, optical terrain navigation is a viable option and has produced positive results in past studies [1–3].

Orion will have star trackers and digital cameras onboard. The two star trackers are required to detect both stars and terrain features on a single image. The digital cameras are primarily designed for proximity operations and docking, but they are potentially usable for surface feature tracking. The star trackers and cameras images will be processed by an onboard digital computer to determine known features on the lunar surface. The position of the features in the image will provide azimuth and elevation information in the camera's own body-fixed frame, which can be used directly by the onboard computer or combined with star tracker data to measure stellar angles. Strategies to include measurements in the onboard navigation filter include:

1. Processing the unit vector obtained from the azimuth and elevation.
2. Processing the apparent angle between a landmark and a known star.
3. Processing the elevation between the lunar horizon and a known star.

While strategies 1 and 2 provide identical information, each have advantages and disadvantages. The elevation between the landmark and a known star is a scalar measurement. As such, it is attitude independent and is therefore immune to attitude estimation errors and camera misalignments. To avoid introducing errors due to relative misalignment between cameras, it is preferable that the same camera capture both the landmark and the star. However, such a solution is strongly limited by the field of view (FOV) of the sensors. The mentioned measurements' sensitivity to the spacecraft's position have inverse proportionality to the distance to the Moon. It is expected that the landmark solutions will perform better closer to the lunar surface (where

*Second Lieutenant, US Air Force. Rice University Graduate Student and Draper Laboratory Fellow, The Charles Stark Draper Laboratory, 17629 El Camino Real, Suite 470, Houston, Texas, 77058. bcrouse@draper.com

†Senior Member of the Technical Staff, GN&C Manned Space Systems, The Charles Stark Draper Laboratory, 17629 El Camino Real, Suite 470, Houston, Texas, 77058. rzanetti@draper.com

‡GN&C Autonomous Flight Systems Engineer, Aeroscience and Flight Mechanics Division, NASA Johnson Space Center EG6, 2101 NASA Parkway, Houston, Texas, 77058. chris.dsouza@nasa.gov

§Professor of Mechanical Engineering and of Civil Engineering, Rice University, 6100 Main Street, Houston, TX 77005, 233 MEB , spanos@rice.edu

it is easier to capture the landmark), while the star-horizon elevation approach will perform better further away from the lunar surface (where it is easier to determine the horizon and the substellar point).

In this paper, models for all the above mentioned measurements are presented, together with trade studies to determine a mission strategy for their utilization. Studies were conducted for two trajectories: low lunar orbit (LLO) and highly elliptical lunar orbit. The Orion LLO is a 100 km trajectory that will be used while the astronauts are on the lunar surface. The high elliptical trajectory is used by Orion during its trans-Earth injection (TEI) 3 burn sequence.

LINEAR COVARIANCE ANALYSIS

The analysis is done with linear covariance (LinCov) techniques [4,5]. It uses linearized error equations to propagate the statistics of the system random variables directly. It has the advantage of obtaining statistical properties of the estimation error in a single run and it is therefore quite useful during the initial stages of navigation system design. Orion is still under development, and many of the vehicle and orbit specifications are continuously changing. LinCov analysis provides capability for rapid analysis of many variations of the navigation parameters.

In spacecraft navigation, an optimal estimator such as the Kalman Filter allows for sequential inclusion of measurement data to improve state information. The system states and the covariances associated with those states are first propagated using a system dynamics model, and then updated sequentially. In linear covariance analysis, the system dynamics are linearized about a nominal trajectory, which, in this particular tool, is found by integrating the system dynamics. The nonzero components of the nominal state are

$$\mathbf{x}_{nom} = \begin{bmatrix} \mathbf{r} & \mathbf{v} & \mathbf{q}_b^i & \boldsymbol{\omega} \end{bmatrix}. \tag{1}$$

The nominal state trajectory can be calculated *a priori* and stored for reference, or it can be calculated in the simulation. This LinCov analysis uses the second method, and the nominal state evolves as

$$\dot{\mathbf{x}}_{nom} = \mathbf{f}\left(\mathbf{x}_{nom}, t\right). \tag{2}$$

The components of the state are inertial position, inertial velocity, body to inertial attitude, and attitude rate. Attitude is propagated as a four component quaternion to avoid singularities which occur in three component attitude representations. The other states represent errors which are nominally equal to zero. Neither a truth (environment) state nor an estimated (onboard filter) state are calculated. Covariances of the differences between states are carried in the simulation. Environment dispersions are the difference between the nominal and truth states:

$$\delta\mathbf{x} = \mathbf{x} - \mathbf{x}_{nom}, \tag{3}$$

assumed to be zero mean with covariance

$$\mathbf{P} = E\left[\delta\mathbf{x}\delta\mathbf{x}^T\right]. \tag{4}$$

Navigated dispersions are the difference between the nominal and filter states:

$$\delta\hat{\mathbf{x}} = \hat{\mathbf{x}} - \mathbf{x}_{nom}, \tag{5}$$

assumed to be zero mean with covariance

$$\hat{\mathbf{P}} = E\left[\delta\hat{\mathbf{x}}\delta\hat{\mathbf{x}}^T\right]. \tag{6}$$

Navigation errors are the difference between the filter and truth states:

$$\mathbf{e} = \mathbf{x} - \hat{\mathbf{x}}, \tag{7}$$

with covariance

$$\mathbf{P}_{onb} = E\left[\mathbf{e}\mathbf{e}^T\right]. \tag{8}$$

The "true" dynamics are not propagated; its model is similar to Eq. (2) with the addition of noise, $\mathbf{w}$, to represent dynamical effects unmodeled by the nominal dynamics. That is,

$$\dot{\mathbf{x}} = \mathbf{f}\left(\mathbf{x}, t\right) + \mathbf{w}(t), \tag{9}$$

where $\mathbf{w}(t)$ is a white noise with zero mean and spectral density given by $\mathbf{Q}$. Linearizing Eq. (9) at the nominal state and neglecting higher order terms results in a first order truth dynamics partial derivative matrix,

$$\mathbf{A} = \left.\frac{\partial \mathbf{f}\left(\mathbf{x}, t\right)}{\partial \mathbf{x}}\right|_{\mathbf{x}_{nom}}, \tag{10}$$

which can be used to propagate the environment dispersion covariance matrix via the Riccati equation

$$\dot{\mathbf{P}} = \mathbf{A}\mathbf{P} + \mathbf{P}\mathbf{A}^T + \mathbf{Q}. \tag{11}$$

Filter dynamics describe how the filter state, which is the estimate of the truth state, will behave. The filter state uses state replacement for angular velocity because those states are measured directly by onboard gyroscopes. Thus, the equations for the filter dynamics differ from the truth dynamics slightly and are given by the equation,

$$\dot{\hat{\mathbf{x}}} = \hat{\mathbf{f}}\left(\hat{\mathbf{x}}, \tilde{\boldsymbol{\omega}}, t\right), \tag{12}$$

where the "hat" notation associates the variables with the filter states. The "tilde" notation denotes variables that are measured directly. The gyroscope introduces noise into the attitude rate states, which shall be modeled as a white noise with zero mean and variance, $\hat{\mathbf{Q}}$.

$$\hat{\mathbf{A}} = \left.\frac{\partial \hat{\mathbf{f}}\left(\hat{\mathbf{x}}, t\right)}{\partial \hat{\mathbf{x}}}\right|_{\mathbf{x}_{nom}} \tag{13}$$

Filter states are not carried in the simulation. Instead, information is propagated in the navigated dispersion covariance matrix via the Riccati equation,

$$\dot{\hat{\mathbf{P}}} = \hat{\mathbf{A}}\hat{\mathbf{P}} + \hat{\mathbf{P}}\hat{\mathbf{A}} + \hat{\mathbf{Q}}. \tag{14}$$

The navigation error is the primary measure of navigation performance. This information is carried in the onboard covariance matrix, which is propagated using the equation,

$$\dot{\mathbf{P}}_{onb} = \hat{\mathbf{A}}\mathbf{P}_{onb} + \mathbf{P}_{onb}\hat{\mathbf{A}} + \mathbf{Q}_{onb}. \tag{15}$$

Dispersions and navigation error covariances grow as time passes as a result of imperfect system models. In general, environment dispersions are reduced by the incorporation of maneuvers and navigation errors are reduced by the incorporation of measurements. True measurements are defined as a function of the true state,

$$\mathbf{z} = \mathbf{h}(\mathbf{x}) + \boldsymbol{\nu}, \tag{16}$$

with measurement noise, $\boldsymbol{\nu}$, white, zero mean, and having variance, $\mathbf{R}$. Nominal measurements are defined by the same function in equation (16) but lack the measurement process noise:

$$\mathbf{z}_{nom} = \mathbf{h}(\mathbf{x}_{nom}). \tag{17}$$

The estimated measurements used in the filter are given as

$$\hat{\mathbf{z}} = \hat{\mathbf{h}}(\hat{\mathbf{x}}). \tag{18}$$

True states are not updated by measurements, because taking a measurement does not change where the spacecraft actually is. The same is true for the nominal states. The purpose of measurements is to update the

filter states and covariances. When the true measurement is different from the estimated measurement in the filter, the filter state should be updated appropriately. That is,

$$\hat{\mathbf{x}}^{+} = \hat{\mathbf{x}}^{-} + \mathbf{K}\left(\mathbf{z} - \hat{\mathbf{z}}\right). \tag{19}$$

The updated estimation error is approximated through linearization, where

$$\mathbf{H} = \left.\frac{\partial \mathbf{h}(\mathbf{x})}{\partial \mathbf{x}}\right|_{\mathbf{x}_{nom}} \tag{20}$$

and

$$\hat{\mathbf{H}} = \left.\frac{\partial \hat{\mathbf{h}}(\hat{\mathbf{x}})}{\partial \hat{\mathbf{x}}}\right|_{\mathbf{x}_{nom}}. \tag{21}$$

Since both partial derivatives are evaluated at the nominal state and subtracted from one another in Eq. (19), the resulting state update equation for the onboard navigation error is

$$\mathbf{e}^{+} = \mathbf{e}^{-} - \mathbf{K}\mathbf{H}\mathbf{e}^{-} - \mathbf{K}\boldsymbol{\nu}. \tag{22}$$

The onboard covariance is updated using the equation,

$$\mathbf{P}^{+}_{onb} = (\mathbf{I} - \mathbf{K}\mathbf{H})\mathbf{P}^{-}_{onb}(\mathbf{I} - \mathbf{K}\mathbf{H}) + \mathbf{K}\mathbf{R}\mathbf{K}^{T}. \tag{23}$$

The gain, K, is known as the Kalman gain and is found by minimizing the weighted scalar sum of the diagonal elements of the error [6],

$$\mathbf{K} = \hat{\mathbf{P}}^{-}\mathbf{H}(\mathbf{H}\hat{\mathbf{P}}^{-}\mathbf{H}^{T} + \mathbf{R})^{-1}. \tag{24}$$

The superscript, "-" denotes a variable that has not been updated, and "+" denotes the updated version of that variable. A full discussion of linear covariance analysis mathematics, Kalman filtering, and how they are applied to the surface feature tracking camera of this work can be found in reference [7].

MEASUREMENT MODELS

Since this paper is concerned with sensor analysis, only the models for the celestial sensors will be presented. The dynamics models used for propagation of the states are unchanged from other works [1, 5, 7]. The same is true for the inertial sensors and other aspects of LinCov. The measurement models developed below are integrated into the existing versions of LinCov and used to analyze and investigate the questions raised in the introduction to this study.

Feature Tracking Camera

The feature tracking camera updates the onboard covariance matrix by processing the measured feature azimuth and elevation. The camera is nominally aligned with the body frame nadir direction. There are several errors associated with this measurement. First, it must be assumed that there is a slight misalignment between the camera and the body frame. This will be represented by a transformation matrix, $\mathbf{T}^{S}_{B}(\boldsymbol{\psi})$. The next error is a camera bias in both azimuth and elevation, b_α and b_δ. The third error is a vector bias in feature position, $\mathbf{b}_F$. The final error is the measurement noise, ν.

The measurement model used is the one developed in [1] and [7]. Specifically,

$$\mathbf{h}(\mathbf{x}) = \begin{bmatrix} \alpha \\ \delta \end{bmatrix} = \begin{bmatrix} \arctan\left(\frac{Y}{X}\right) + b_\alpha + \nu \\ \arcsin\left(Z\right) + b_\delta + \nu \end{bmatrix}, \tag{25}$$

where

$$\begin{bmatrix} X \\ Y \\ Z \end{bmatrix} = \frac{\mathbf{T}^{s}_{b}\mathbf{T}^{b}_{i}\left[\mathbf{T}^{i}_{p}(\mathbf{r}_F + \mathbf{b}_F) - \mathbf{r}\right]}{\rho}, \tag{26}$$

Furthermore, the symbols X, Y, and Z represent the components of the vector defined in Eq. (26). $\mathbf{T}_i^b$ is a transformation from inertial to body, and $\mathbf{T}_p^i$ is the transformation from the planet fixed frame to the inertial frame. The feature position, $\mathbf{r}_F$, is constant in the planet fixed frame, and is rotated to the inertial frame to process the measurement. The vector, $\mathbf{r}$, is the spacecraft position, and ρ is the magnitude of the numerator in Eq. (26). The measurement partial derivative matrix is

$$\mathbf{H} = \begin{bmatrix} \frac{\partial \alpha}{\partial \mathbf{r}} & \frac{\partial \alpha}{\partial \boldsymbol{\phi}} & \frac{\partial \alpha}{\partial \boldsymbol{\psi}} & \frac{\partial \alpha}{\partial b_\alpha} & 0 & \frac{\partial \alpha}{\partial \mathbf{b}_F} \\ \frac{\partial \delta}{\partial \mathbf{r}} & \frac{\partial \delta}{\partial \boldsymbol{\phi}} & \frac{\partial \delta}{\partial \boldsymbol{\psi}} & 0 & \frac{\partial \delta}{\partial b_\delta} & \frac{\partial \delta}{\partial \mathbf{b}_F} \end{bmatrix}, \tag{27}$$

with

$$\frac{\partial \alpha}{\partial \mathbf{r}} = -\frac{1}{\rho \cos(\delta)} \begin{bmatrix} -\sin(\alpha) & \cos(\alpha) & 0 \end{bmatrix} \mathbf{T}_i^s,$$

$$\frac{\partial \alpha}{\partial \boldsymbol{\phi}} = \frac{1}{\rho \cos(\delta)} \begin{bmatrix} -\sin(\alpha) & \cos(\alpha) & 0 \end{bmatrix} \mathbf{T}_b^s \frac{d\mathbf{T}_i^b \mathbf{r}}{d\boldsymbol{\phi}},$$

$$\frac{\partial \alpha}{\partial \boldsymbol{\psi}} = \frac{1}{\rho \cos(\delta)} \begin{bmatrix} -\sin(\alpha) & \cos(\alpha) & 0 \end{bmatrix} \frac{d\mathbf{T}_b^s \mathbf{r}^b}{d\boldsymbol{\phi}},$$

$$\frac{\partial \alpha}{\partial b_\alpha} = 1,$$

$$\frac{\partial \alpha}{\partial \mathbf{b}_F} = \frac{1}{\rho \cos(\delta)} \begin{bmatrix} -\sin(\alpha) & \cos(\alpha) & 0 \end{bmatrix} \mathbf{T}_i^s \mathbf{T}_p^i,$$

$$\frac{\partial \delta}{\partial \mathbf{r}} = -\frac{1}{\rho} \begin{bmatrix} -\cos(\alpha)\sin(\delta) & -\sin(\alpha)\sin(\delta) & \cos(\delta) \end{bmatrix} \mathbf{T}_i^s,$$

$$\frac{\partial \delta}{\partial \boldsymbol{\phi}} = \frac{1}{\rho} \begin{bmatrix} -\cos(\alpha)\sin(\delta) & -\sin(\alpha)\sin(\delta) & \cos(\delta) \end{bmatrix} \mathbf{T}_b^s \frac{d\mathbf{T}_i^b \mathbf{r}}{d\boldsymbol{\phi}},$$

$$\frac{\partial \delta}{\partial \boldsymbol{\psi}} = \frac{1}{\rho} \begin{bmatrix} -\cos(\alpha)\sin(\delta) & -\sin(\alpha)\sin(\delta) & \cos(\delta) \end{bmatrix} \frac{d\mathbf{T}_b^s \mathbf{r}^b}{d\boldsymbol{\phi}},$$

$$\frac{\partial \delta}{\partial b_\delta} = 1,$$

and

$$\frac{\partial \delta}{\partial \mathbf{b}_F} = \frac{1}{\rho} \begin{bmatrix} -\cos(\alpha)\sin(\delta) & -\sin(\alpha)\sin(\delta) & \cos(\delta) \end{bmatrix} \mathbf{T}_i^s \mathbf{T}_p^i.$$

The values for the biases and measurement noise used in the simulation are summarized in Table (1).

Error Type	1σ Value	Units
Misalignment	0.1	deg
Bias in α, β	0.1	deg
Feature Bias	20	m
Measurement Noise	0.0002	rad

Table 1. Feature Tracking Camera Errors

Star Landmark Sensor

The star landmark sensor measures the angle A between the landmark of interest, and a star. The theory for the development of this sensor comes from [8]. The advantage of using this sensor instead of the feature tracking camera is that the seperation angle is a scalar quantity. Therefore, this sensor's measurement is independent of attitude and alignment errors. It is advantageous to detect landmark features close to the vehicle's nadir. This strategy would guarantee that the features are closer and especially would decrease optical deformation of the craters making them more easily recognized. Unfortunately it is unlikely that the camera with field of view large enough to capture both a star and a landmark close to nadir would be installed on Orion. In LLO, the camera would need a field of view greater than 143 degrees. Therefore, the landmark would be viewed in the optical camera, and the stars would be viewed by a startracker that is installed on Orion in a direction normal to the optical camera. This configuration introduces a misalignment between the two cameras, which must be taken into account. However, the measurement is still independent of attitude.

There are various errors associated with the star landmark sensor. The first is the misalignment between cameras, $\mathbf{T}(\gamma)$. There also are biases in azimuth, elevation, and feature position, as before. The overall star camera bias, b_{sc} is also modeled. The last error source is the sensor measurement noise, η_{sc}. Note that there is no correction for aberration effects in the model. It is assumed that since orbital trajectory speeds are much slower than that of cislunar trajectories, they can be ignored. The model is

$$h(\mathbf{x}) = A = \arccos\left(\hat{\imath}_s^T \mathbf{T}(\gamma)\hat{\imath}_{VL}\right) + b_{sc} + \eta_{sc}, \tag{28}$$

where

$$\hat{\imath}_{VL} = \begin{bmatrix} \cos(\alpha + b_\alpha)\cos(\delta + b_\delta) \\ \sin(\alpha + b_\alpha)\cos(\delta + b_\delta) \\ \sin(\delta + b_\delta) \end{bmatrix}, \tag{29}$$

$$\alpha = \arctan\left(\frac{Y}{X}\right),$$

$$\delta = \arcsin(Z),$$

and

$$\begin{bmatrix} X \\ Y \\ Z \end{bmatrix} = \frac{\mathbf{T}_P^I(\mathbf{r}_F + \mathbf{b}_F) - \mathbf{r}}{\rho}.$$

The measurement partial matrix is

$$\mathbf{H} = \begin{bmatrix} \frac{\partial A}{\partial \mathbf{r}} & \frac{\partial A}{\partial \boldsymbol{\gamma}} & \frac{\partial A}{\partial b_\alpha} & \frac{\partial A}{\partial b_\delta} & \frac{\partial A}{\partial \mathbf{b}_F} & \frac{\partial A}{\partial b_{sc}} \end{bmatrix}, \tag{30}$$

with

$$\frac{\partial A}{\partial \mathbf{r}} = \frac{1}{\rho \sin(A)}\left[\hat{\imath}_s^T \mathbf{T}(\boldsymbol{\gamma}) - \cos(A)\hat{\imath}_{VL}^T\right],$$

$$\frac{\partial A}{\partial \boldsymbol{\gamma}} = \frac{1}{\sin(A)}\hat{\imath}_s^T[\hat{\imath}_{VL}\times],$$

$$\frac{\partial A}{\partial b_\alpha} = -\frac{1}{\sin(A)}\hat{\imath}_s^T \mathbf{T}(\boldsymbol{\gamma}) \begin{bmatrix} -\sin(\alpha + b_\alpha)\cos(\delta + b_\delta) \\ \cos(\alpha + b_\alpha)\cos(\delta + b_\delta) \\ 0 \end{bmatrix},$$

$$\frac{\partial A}{\partial b_\delta} = -\frac{1}{\sin(A)}\hat{\imath}_s^T \mathbf{T}(\boldsymbol{\gamma}) \begin{bmatrix} -\cos(\alpha + b_\alpha)\sin(\delta + b_\delta) \\ -\sin(\alpha + b_\alpha)\sin(\delta + b_\delta) \\ \cos(\delta + b_\delta) \end{bmatrix},$$

$$\frac{\partial A}{\partial \mathbf{b}_F} = -\frac{1}{\rho \sin(A)}\left[\hat{\imath}_s^T \mathbf{T}(\boldsymbol{\gamma}) - \cos(A)\hat{\imath}_{VL}^T\right]\mathbf{T}_p^i,$$

and

$$\frac{\partial A}{\partial b_{sc}} = 1,$$

where

$$\cos(A) = \hat{\imath}_s^T \mathbf{T}(\boldsymbol{\gamma}) \hat{\imath}_{VL}, \tag{31}$$

and $[\hat{\imath}_{VL}\times]$ is the notation for a skew symmetric matrix of the included vector. In order to calculate the partial with respect to the misalignment vector, the following small angle first order approximation for a transformation matrix is made:

$$\mathbf{T}(\boldsymbol{\gamma}) = \mathbf{I} + [\boldsymbol{\gamma}\times]. \tag{32}$$

This result is obtained from [9] with the sign changed due to the fact that LinCov uses a left handed quaternion and rotation convention. The values for the errors are given in Table (2).

Error Type	1σ Value	Units
Camera Misalignment	0.1	deg
Bias in α, β	0.1	deg
Feature Bias	20	m
Camera Bias	5	arcsec
Measurement Noise	3.35	arcsec

Table 2. Star Landmark Sensor Errors

Star Horizon Sensor

The model for the star-horizon measurement is based on [10]. The apparent direction of the star is given by $\mathbf{i}_s$. The apparent direction of the horizon is given by the equation,

$$\mathbf{i}_h = \mathrm{Unit}(\mathbf{r}_h - \mathbf{r}) \tag{33}$$

where the notation $\mathrm{Unit}(\mathbf{v})$ means the unit vector with the same direction of vector $\mathbf{v}$. The vector, $\mathbf{r}$, is the position of the spacecraft, and $\mathbf{r}_h$ is the position of the substellar point on the horizon. The perfect star-elevation measurement is given by the equation,

$$y_{se}^\star = \arccos(\mathbf{i}_h \cdot \mathbf{i}_s). \tag{34}$$

Three error sources are modeled, each having both bias and noise. The first source of error is the precision of the star camera. The noise is η_{sc} and the bias is b_{sc}. The second source of error is the identification of the substellar point along the planet's horizon, with bias b_{ss} and noise η_{ss}. Finally, there is the error in determining the altitude of the horizon, whose bias is b_h and noise is η_h. The measurement model is obtained using the cosine law and is given by the equation

$$\begin{aligned} y_{se} = \Bigg\{ &\left(y_{se}^\star + \arcsin\frac{R_p}{r_{pv}}\right)^2 + \left(\arcsin\frac{R_p}{r_{pv}} + \arcsin\frac{b_h+\eta_h}{r_{pv}}\right)^2 + \\ &- 2\left(y_{se}^\star + \arcsin\frac{R_p}{r_{pv}}\right)\left(\arcsin\frac{R_p}{r_{pv}} + \arcsin\frac{b_h+\eta_h}{r_{pv}}\right)\cos(b_{ss}+\eta_{ss})\Bigg\}^{\frac{1}{2}} + b_{sc} + \eta_{sc}, \end{aligned} \tag{35}$$

where R_p is the planet's diameter and r_{pv} is the distance between the planet and the vehicle. The nominal measurement is given by the equation

$$\bar{y}_{se} = \left\{ \left(\bar{y}^{\star}_{se} + \arcsin \frac{R_p}{\bar{r}_{pv}} \right)^2 + \left(\arcsin \frac{R_p}{\bar{r}_{pv}} + \arcsin \frac{\bar{b}_h}{\bar{r}_{pv}} \right)^2 + \right. \tag{36}$$

$$\left. - 2 \left(\bar{y}^{\star}_{se} + \arcsin \frac{R_p}{\bar{r}_{pv}} \right) \left(\arcsin \frac{R_p}{\bar{r}_{pv}} + \arcsin \frac{\bar{b}_h}{\bar{r}_{pv}} \right) \cos \bar{b}_{ss} \right\}^{\frac{1}{2}} + \bar{b}_{sc}. \tag{37}$$

The measurement mapping matrix and the noise shaping matrix are defined as

$$\mathbf{H}_{se} = \left. \frac{\partial y_{se}}{\partial \mathbf{x}} \right|_{\mathbf{x}=\bar{\mathbf{x}}, \boldsymbol{\eta}_{se}=\mathbf{0}} \qquad \mathbf{L}_{se} = \left. \frac{\partial y_{se}}{\partial \boldsymbol{\eta}_{se}} \right|_{\mathbf{x}=\bar{\mathbf{x}}, \boldsymbol{\eta}_{se}=\mathbf{0}}, \tag{38}$$

where

$$\boldsymbol{\eta}_{se} = \begin{bmatrix} \eta_{st} \\ \eta_{ss} \\ \eta_h \end{bmatrix}, \tag{39}$$

and

$$\mathbf{R}_{se} = \mathbf{L}_{se} \, \mathrm{E} \left\{ \boldsymbol{\eta}_{se} \boldsymbol{\eta}_{se}^{\mathrm{T}} \right\} \mathbf{L}_{se}^{\mathrm{T}}. \tag{40}$$

The partials and a more detailed derivation are presented in Ref. [10].

TEST METHODOLOGY

Since the star landmark and star horizon sensors are fundamentally the same, it is worth examining which point on the planet will result in the highest measurement sensitivity. That is, all errors being equal, is it better to select a surface landmark which is very close to the center of the planet, or the horizon sub-stellar point, which is the edge of the planet? Which measurement theoretically reduces position navigation error further?

The two main trajectory scenarios explored in this paper have vastly different parameters. In the LLO trajectory, Orion will loiter over the lunar surface at a constant altitude of 100 km for multiple orbits. In the TEI trajectory, Orion will perform a burn to place itself in a highly elliptical orbit with a maximum altitude of almost 16,000 km. Throughout the course of the TEI sequence, Orion will need to continue taking navigation measurements. Since each sensor measurement presented in this paper is sensitive to spacecraft altitude, it is also worth examining the error sources to decide whether one sensor would be better than another in different altitude regions.

The feature tracking camera measurement will not be very accurate at altitudes far above the surface because the limited resolution of the camera will make the landmarks difficult to track. The star landmark camera has similar error sources to the feature tracking camera. It, too, is expected to be more accurate at low altitudes. The star horizon camera ought to be the more accurate sensor at higher altitudes because its errors are based on distinguishing the sub-stellar point, which is easier to distinguish at higher altitudes. The altitude threshold beyond which one sensor is better than the other is be found by comparing the steady state performance of the navigation system using each of the sensors.

Test Cases

To answer the two preceeding questions, multiple LinCov runs are set up and run. Nominally, LinCov has a gyroscope and startracker sensor, which measure spacecraft angular velocity and attitude. They will remain enabled for all simulations because they do not affect position error. The performance of the feature tracking optical camera has been documented extensively in [7]. To better detect the individual differences between processing a landmark and the horizon, the optical camera will be turned off for these simulations.

Figure 1 shows an example plot of a single run in LinCov. This plot shows the 3σ root sum square of

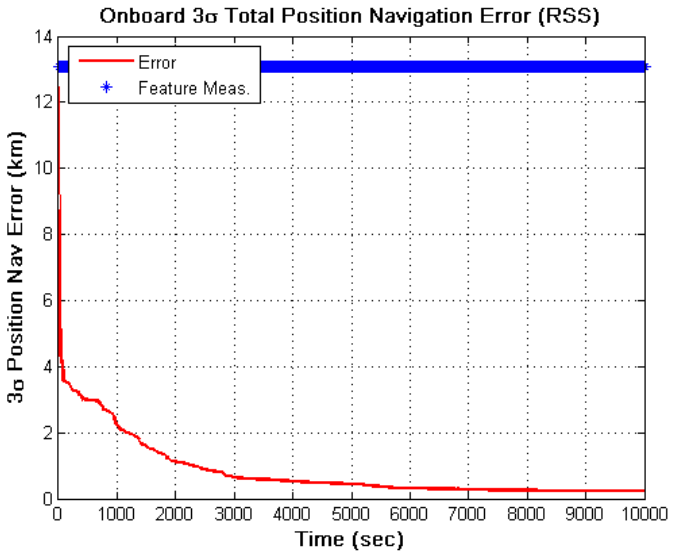

Figure 1. Star Landmark Sensor, 500km Orbit

position navigation error, calculated from the onboard covariance matrix,

$$\sigma_{pos} = 3\sqrt{\mathbf{P}_{onb}(1,1) + \mathbf{P}_{onb}(2,2) + \mathbf{P}_{onb}(3,3)} \tag{41}$$

as a function of time. LinCov was initialized with Orion in a 500 km equatorial circular orbit starting at the first point of Aries. Integration was performed with a 10 second step size, and the sensors were configured with the optical sensor being the star landmark sensor processing two stars simultaneously with the same landmark. The error starts high but quickly drops to a steady state level while the navigation error covariance matrix continuously updates with sensor measurements.

Figure (2) shows an example plot of a TEI sequence run. It provides position navigation error in local vertical local horizontal (LVLH) coordinates. In this case, a maneuver at 2.7 hours raises the orbit, and the error increases steadily as the spacecraft approaches an apogee of 16000 km. At 17.8 hours, another maneuver initiates a plane change, and the sequence ends at 26.7 hours once the spacecraft reaches a perigee of 100 km. The star horizon sensor is the optical sensor processing two stars, and the run used a 100 second step size.

Various parameters in the sensor configurations are changed to create an appropriate ensemble of results and plots in order to derive answers to each of the preceeding questions. The tests and their results are summarized in the following section.

RESULTS

The first question to be addressed is the one of optimal location on the planet to use as the landmark. The angle processed in the star landmark and star horizon sensors is an inner product between two unit vectors. In all of the following runs, the star is selected from a table of 165 stars based on which star is closest to 45 degrees above the horizon. A pre-defined unit vector can be used in conjunction with the star table to determine the best location for the landmark. Nominally, the current landmark being processed by the feature tracking camera is used as the landmark unit vector. For testing purposes, however, locations were selected at nadir (i.e. the center of the planet), the horizon, 1/3 the way to the horizon, and 2/3 of the way to the horizon. See Figure 3.

Figure 4 shows the results of running the TEI sequence with the generic star camera choosing each of the four locations specified in Figure 3. The generic star camera sensor had only a single source of error, which

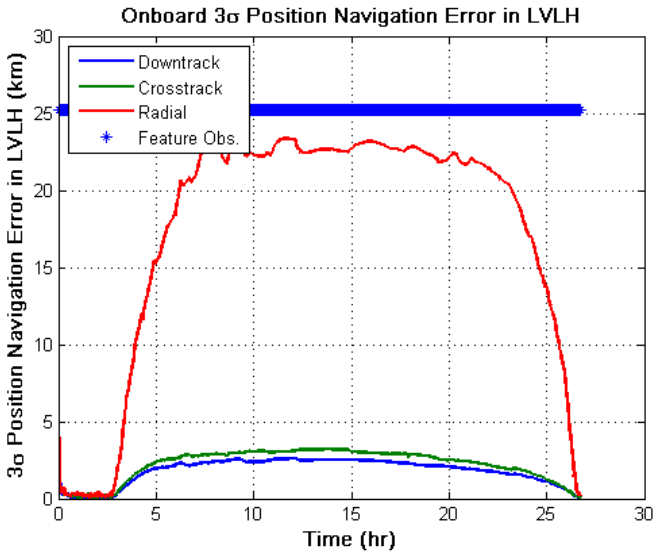

Figure 2. Star Horizon Sensor, TEI Sequence

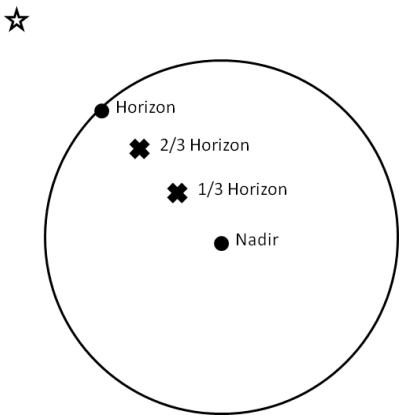

Figure 3. Apparent View of Lunar Sphere

is a camera measurement noise that remained the same in each of the four test cases.

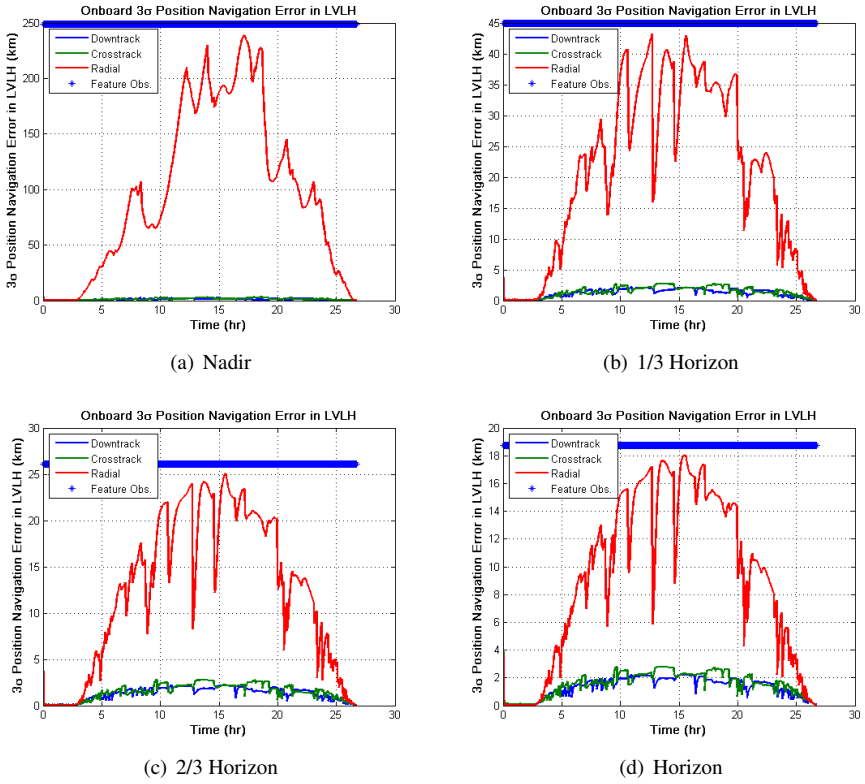

(a) Nadir

(b) 1/3 Horizon

(c) 2/3 Horizon

(d) Horizon

Figure 4. TEI Runs With a Generic Star Camera

As the landmark location moves from the center of the planet to the horizon, the maximum error decreases. With all other errors being equal, processing a star horizon measurement is much more accurate than processing a star nadir measurement. In fact, the greatest drop in error occurs between the nadir direction and the direction to 1/3 horizon. The largest component of position error is in the radial direction. Indeed, the other components of error are actually quite similar in each of the four landmark locations. The reason for the difference in position uncertainty is geometric. Consider Figure 5.

In this diagram, all angles are measured from the center of the planet (nadir). The angle subtended by the lines of sight to the nadir direction and the star form a cone in space with the spacecraft on the surface. The center of the planet is the apex of the cone whose center axis is the line of sight between the planet and the star. The angle of the cone is twice the supplement of the measured elevation angle. The intersection of this cone with another cone formed about a second star establishes a line of position on which the spacecraft rests. Any additional stars will only confirm the line of position already established by the first two stars. Therefore, when nadir is processed as the landmark, regardless of where the star is, no information about the radial distance from the planet is added to the filter. Now consider Figure (6).

In this diagram, angles are measured from the substellar point to the star instead of the center of the planet. Therefore, stars at different locations will generate position cones that have different apices. Now, intersections between two cones result in points in space instead of lines. Using this method, position uncertainty is further reduced than in the case of Figure (5) because information about spacecraft radial distance is processed in the filter. Three stars are shown because the intersection of two cones actually makes two points. The third star selects the correct point as measured position. Thus, three pieces of information are required for a position fix. The further the landmark is from the center of the planet, the more information about the

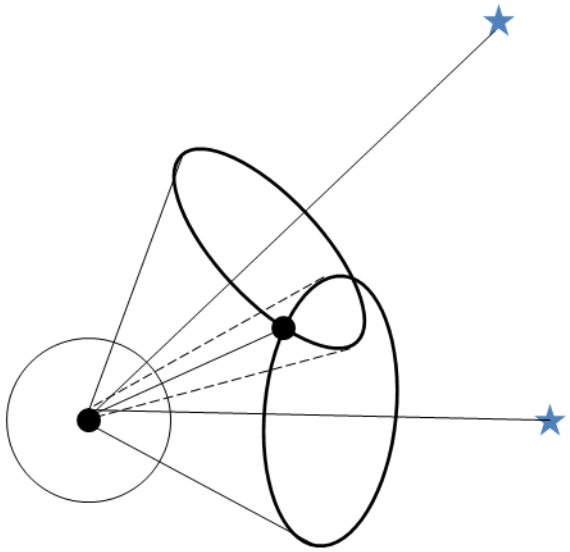

Figure 5. Geometry of a Position Fix (Nadir)

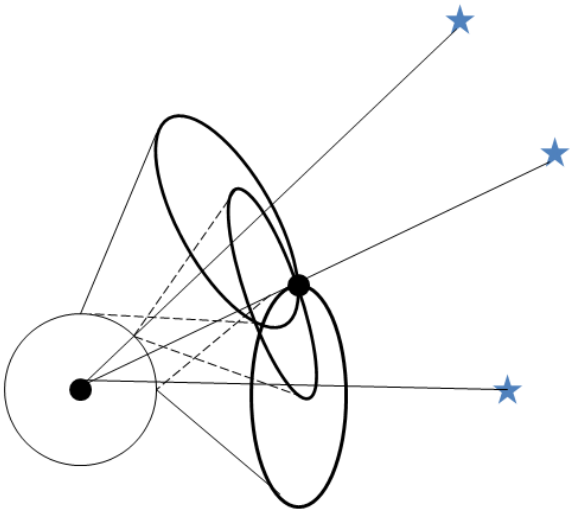

Figure 6. Geometry of a Position Fix (Horizon)

radial direction is added, so the total position error is lower.

When actual landmarks are used in the star landmark measurement, they are selected based on which one is closest to the nadir direction. They will never be exactly in the nadir direction; thus, certain information concerning the radial component of error will be added to the filter. Nonetheless, the star horizon sensor is the more accurate sensor.

As discussed in the introduction to this section, the next step is to determine at which altitude the star horizon sensor becomes more accurate than the star landmark sensor. For this purpose, plots like Figure 1 are created based on circular orbits with different altitudes. If the average value of error is taken once the plot reaches steady state (after about 6000 seconds in Figure 1), one data point for position navigation error versus altitude is created. In Figure 1, a 500 km orbit generates a steady state error of 0.092 km. The altitude range of interest stretches between orbits of 100 km to 16000 km. Figure 7 shows the position accuracy obtained by

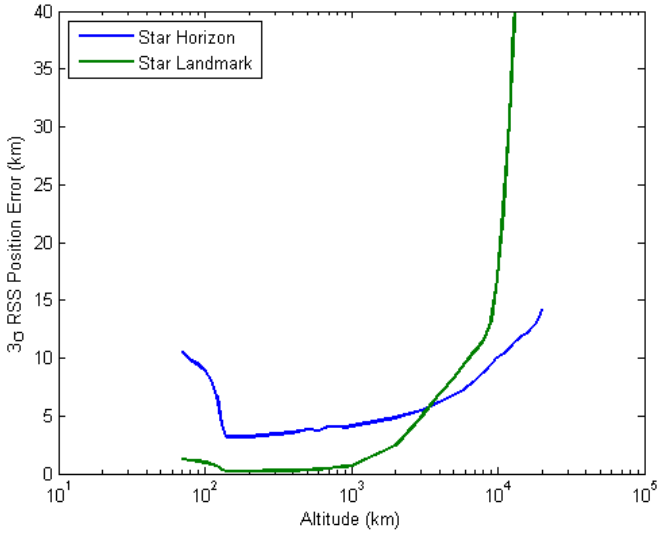

Figure 7. Star-Landmark vs. Star-Horizon Performance

processing the two types of star elevation measurements with a 100 second step size. Circular plots ranging from 75 km to 20000 km were used to fully populate the plot. Since dozens of plots were created to produce these data points, they are omitted for the sake of space. Their behavior is all very similar to Figure 1, with different steady state values. The number of data points near LLO and near the crossover point is denser to provide greater resolution. The two lines show elevation measurements from the landmark and the horizon. At low altitudes, processing landmarks is preferable, while at higher altitudes horizon elevation measurements are recommended.

Since the star landmark camera essentially gives the same information as the feature tracking camera, it is worth asking why one would use a star landmark camera at all. It is thought that the removal of attitude dependency might warrant use of the star landmark camera. How do the two cameras compare? Figure 8 shows how the cameras compare throughout the range of altitudes. Also included in Figure 8 is a plot of the star landmark sensor with no misalignment error included in the model. This plot would simulate a camera capable of capturing both the landmark and the star in the same image. Naturally, it has better accuracy than the original camera model; however, it is only significant after the range at which the CEV would have switched to the star horizon sensor.

At low altitudes (below 130 km) the error starts high and then drops down before resuming the expected behavior for both sensors. This behavior is due to the lunar gravity perturbations. Currently, Earth gravity models are very accurate in comparison to lunar models. Not only does Earth have a much more stable

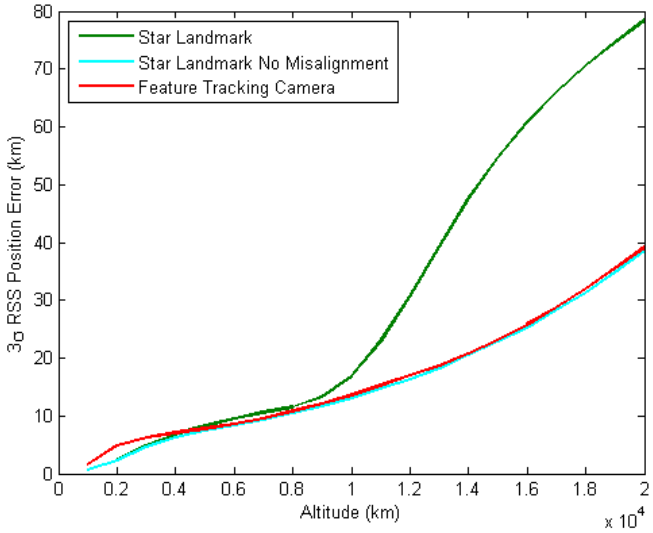

Figure 8. Star Landmark vs. Feature Tracking

gravity field, but it has also been documented in more detail over the years due to the far greater number of missions. Typically a gravity model accounting for nonspherical parameters up to J4 is sufficiently accurate and computationally efficient for spacecraft in Earth orbit. However, as the few lunar missions have revealed, this same modeling does not sufficiently account for the true effects in lunar orbit, which are due to asymmetric mass concentrations. Therefore, in LinCov, three gravity perturbation states are added to the state matrix. These states are used to approximate errors as if the CEV were carrying a 9x9 gravity model. Figure 9 shows a plot of the position error through a range of LLO altitudes with the gravity perturbation states turned off in LinCov. These runs were also done with a 10 second step size for further clarity. In this

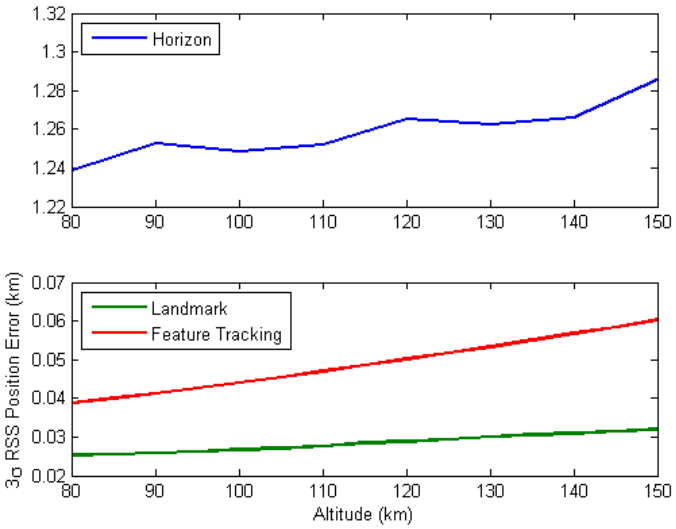

Figure 9. Sensor Performance with No Gravity Perturbations

case, error is smallest at the lowest altitude and increases as altitude increases, as expected. The orbital effect

of the gravity perturbations is more pronounced at LLO, which is the reason for the unexpected behavior at low altitude in Figure 7.

CONCLUSIONS

The final version of the Orion Crew Exploration Vehicle will likely have several optical cameras at its disposal. Since crew safety is of utmost importance, every available resource must be investigated as an aid to returning the crew home in the event of an emergency. Although primary navigation will be handled though ground updates, autonomous optical navigation as presented will likely be the backup navigation system in lunar orbit. The three strategies for including optical measurements in the navigation filter are all useful and viable options. The surface feature tracking capability will likely stay the primary optical measurement. The research has shown, however, that in situations where Orion departs LLO and enters highly elliptical orbits, a star elevation measurement becomes quite helpful in lowering position error. Selecting a landmark off of the nadir direction is ideal. The resolution of the cameras and the altitude above the surface will ultimately determine whether to use the current surface feature or the horizon as the landmark.

REFERENCES

[1] M. Osenar, F. Clark and C. D'Souza, "Performancs of an Automated Feature Tracking Lunar Navigation System," *AAS/AIAA Space Flight Mechanics Meeting*, Galveston, TX, 27-31 January 2008.

[2] K. J. DeMars and R. H. Bishop, "Precision Descent Navigation for Landing at the Moon," *AAS/AIAA Astrodynamics Specialist Conference*, Mackinac Island, MI, August 19–23 2007.

[3] C. C. van Damme and T. Prieto-Llanos and J. Gil-Fernandez, "Optical Navigation for Lunar Transportation Systems Contingency Scenarios," *AIAA/AAS Astrodynamics Specialist Conference and Exhibit*, Honolulu, HI, 18-21 August 2008.

[4] Mayback, P. S., *Stochastic Models, Estimation, And Control Volume 1*, Mathematics in Science and Engineering, Academic Press, Orlando, FL, 1979.

[5] D. K. Geller, "Linear Covariance Techniques for Orbital Rendezvous Analysis and Autonomous Onboard Mission Planning," *Journal of Guidance Control and Dynamics*, Vol. 29, November-December 2006, pp. 1404–1414.

[6] A. Gelb, ed., *Applied Optimal Estimation*. Cambridge, MA: The MIT press Massachusetts Institute of Technology, 1996.

[7] M. Osenar, "Performance of Automated Feature Tracking Cameras for Lunar Navigation," M.S. Thesis, Department of Mechanical Engineering, Rice University, Apr. 2007.

[8] R. H. Battin, *An Introduction to the Mathematics and Methods of Astrodynamics*. American Institute of Aeronautics and Astronautics, New York, NY, 1987.

[9] P. G. Savage, "Strapdown Inertial Navigation Integration Algorithm Design Part 1: Attitude Algorithms," *Journal of Guidance, Control, and Dynamics*, Vol. 21 January-February 1998.

[10] Renato Zanetti. Autonomous mid-cousrse navigation for lunar return. In *Proceedings of the 2008 Astrodynamics Specialist Conference*, Honolulu, Hawaii, August 18–21 2008. AIAA/AAS.